BRILL

IAWA Journal 46 (4), 2025: 535-550

iawa

Development of an automated radial scanning microscopy-based imaging system and its use for measuring resin canal size and frequency in *Pinus taeda*

Nawa Raj Pokhrel [1], Joseph Dahlen [1,*], Thomas L. Eberhardt [2] and Kamal J.K. Gandhi [1]

[1] *D.B. Warnell School of Forestry and Natural Resources, University of Georgia, 180E. Green Street, Athens, GA 30602, USA*
[2] *USDA Forest Service, Forest Products Laboratory, One Gifford Pinchot Drive, Madison, WI 53726, USA*
**Corresponding author; email: jdahlen@uga.edu*
ORCID iDs: Pokhrel: 0000-0003-3605-4521; Dahlen: 0009-0002-7231-4845; Eberhardt: 0000-0002-8818-4822; Gandhi: 0000-0001-6217-5859

Accepted for publication: 23 August 2024; published online: 1 October 2024

Summary – Resin canals produce and transport oleoresins that are important for tree defenses within the Pinaceae family. Rapid measurement techniques are needed to better understand how resin canal characteristics vary due to genetic and environmental effects. Here we describe a semi-automated microscopy imaging system that was built for quantifying longitudinal resin canals. Tree increment cores from 210 loblolly pine (*Pinus taeda* L.) trees were prepared into radial strips and the transverse surface of the samples polished with 400 and then 600 grit sandpaper. Each sample was imaged along its entire length (pith to bark) with the images collected from a monochrome camera connected to a Plan Fluorite 4× objective lens. The samples were imaged on the transverse surface via transmitted 850 nm near-infrared light directed at the radial surfaces of the samples. A total of 24 153 images were collected and then processed offline in Python using the Open Computer Vision Library (OpenCV) using a series of algorithms including contrast correction, noise removal, thresholding, contour identification, erosion, and dilation. A total of 24 491 resin canals were identified and their size quantified. The resin canals were assigned into annual rings and positioned within the earlywood or latewood of a ring using cross-correlation whereby a pseudo-density value was derived from the images and matched with density values measured by X-ray densitometry. Of the total resin canals identified, 51.5% were in the earlywood and 48.5% in the latewood, with the majority being detected in the earlywood in the first six years and the latewood in years 7 and above. This study represents the most information collected on the resin canals of loblolly pine. The detailed description of the hardware and image analysis methods should serve as a useful guide to others interested in imaging resin canals as well as other anatomical features.

Keywords – loblolly pine, nondestructive evaluation, resin ducts, tree defense mechanisms, wood anatomy, wood and fiber quality.

Introduction

Resin (oleoresin) is a complex mixture of terpenoids, resin and fatty acids, waxes, and phenolic compounds transported via resin canals to provide chemical and physical defenses (Sjöström 1993; Raffa 2014) to various genera within the Pinaceae family; these genera include *Cathaya*, *Larix*, *Picea*, *Pinus* and *Pseudotsuga* (LaPasha & Wheeler 1990; Krokene *et al.* 2008). A resin canal complex consists of a resin canal, epithelial cells and subsidiary cells (Wiedenhoeft & Miller 2002; Richter *et al.* 2004). Epithelial cells surround the canal and secrete resin into the lumen of the canal (Wu & Hu 1997; Evert 2006). The subsidiary cells surround the epithelial cells and provide

DOI 10.1163/22941932-bja10169

structural support to the canal, but despite having a structural function, they may later be crushed as the canal widens (Kibblewhite & Thompson 1973; Cabrita 2018). Resin canals are formed in two ways: constitutive resin canals provide a proactive defense system, while traumatic resin canals provide a reactive defense system to an event such as wounding (Lombardero *et al.* 2000; Bollschweiler *et al.* 2008; Krokene *et al.* 2008; Krokene & Nagy 2012; DeRose *et al.* 2017). In the *Abies*, *Cedrus*, *Sequoia* and *Tsuga* genera, traumatic resin canals can be formed as a reactive defense mechanism against environmental disturbances (Wu 1997; Kane *et al.* 2010; Cabrita 2018, 2021).

In secondary xylem, resin canals are oriented both longitudinally (axial resin canals) and horizontally (radial resin canals) along the tree bole, and these two types allow for resin to be transported throughout the stem (Blanche *et al.* 1992; Arbellay *et al.* 2014). Axial and radial resin canals can appear to be connected but are typically separated by common epithelial cells (Bosshard & Hug 1980; LaPasha & Wheeler 1990; Zhang *et al.* 2008). The total resin canal volume in a tree depends on their size and frequency, and therefore, the amount of resin stored within a tree available for excretion in response to wounding varies (Rodríguez-García 2014; Hood & Sala 2015). Axial resin canals are generally larger and form more frequently than radial resin canals (Zhao & Erbilgin 2019; Hood *et al.* 2020; Vázquez-González *et al.* 2020). In *Pinus* species, axial resin canals are typically large enough to be visible to the naked eye (60-300 μm) (Larson 1994; Ruffinatto *et al.* 2023). Resin canals are generally smaller in the other genera as follows: *Larix* (40-80 μm), *Picea* (40-70 μm), and *Pseudotsuga* (40–45 μm) (Larson 1994). In the genus *Pinus*, the frequency of axial resin canals (4–5 canals/mm^2) is more than twice that in the radial direction (0.5–2 canals/mm^2). Focusing on the axial resin canals, their frequency is lower for the other genera as follows: *Cathaya* (0.32 canals/mm^2), *Larix* (2.5–2.8 canals mm^2) and *Picea* (2.4–3.5 canals/mm^2) (Koch 1972; Cabrita 2021).

Quantification of resin canal size and/or frequency is of considerable interest to many different disciplines, including quantifying resin canal formation in relation to phenotyping genetic variability (Levkoev *et al.* 2017; Neis *et al.* 2019; Fabián-Plesníková 2021), determining the effects of silvicultural treatments (Knebel *et al.* 2008; Beleko *et al.* 2021), and measuring changes as a response to abiotic and biotic disturbances (Susilowati & Rachmat 2018; Catherwood *et al.* 2022). An important consideration when quantifying the size and frequency of resin canals in a group of specimens is how to tailor the methodology to efficiently image the resin canals to a sufficient resolution allowing size measurements in addition to their frequency. Imaging protocols generally involve sample preparation, image acquisition, image processing, feature identification, and data extraction (Nixon & Aguado 2019). For resin canals, the first two steps are especially critical to achieve quality images needed for the latter three steps involving the use of image processing software. To date, the most common methods for imaging resin canals have used either flatbed scanners for larger samples prepared by sanding (Chen *et al.* 2008; Thomas & Collins 2017; Hood *et al.* 2020), or microscopy of small wood sections prepared by using a microtome (Gärtner *et al.* 2015; Guillén *et al.* 2017; Chauhan *et al.* 2022). Flatbed scanners are generally used to image a larger sample area than microscopy: this allows for more resin canals to be detected at a time, but due to the lower resolution, measuring the size of the canals can be challenging, with smaller resin canals being difficult to detect at all (Griffin *et al.* 2021). The challenge with traditional microscopy operations is the extremely tedious and time-consuming process of sequentially preparing microtomed samples, compounded by handling issues arising from the inherent fragility of these thin samples (1–60 μm) (Verhertbruggen *et al.* 2017).

An innovative approach to imaging resin canals would be to still retain the resolution afforded by microscopy, but to prepare the samples in a manner that does not require their segmentation for microtome sectioning. To this end, the methods used in the development of the SilviScan system are of particular interest whereby increment cores (or pith-to-bark wood strips cut from disks) are cut to give a 2 mm tangential by 7 mm longitudinal sample along the entire length of wood core or radial strip of wood (Evans 1994; Chen & Evans 2005, 2010; Schimleck *et al.* 2019). Cut samples are prepared for imaging by sanding the transverse surface with a progressive series of sandpapers. For softwoods, the transverse surface of the sample is illuminated by applying longer wavelength light (650–880 nm) to the radial surfaces of the sample. The resulting image is that of bright cell walls and dark lumens, with wood dust (via sanding) in the lumens contributing to the contrast between the cell walls and the cell lumens (Evans 1994). Alternatively, some applications, such as imaging vessels in Eucalyptus trees, still require the use of reflected light rather than transmitted light (Chen & Evans 2005). The general approach of transmitted light utilized by Evans (1994) was adapted by Vahey *et al.* (2007) whereby they built a prototype instrument they called the "Ring Profiler", which was used to quantify tracheid dimensions on a small number of samples.

In this paper, we describe a methodology to image and then measure both frequency and sizes of the axial resin canals for a set of loblolly pine (*Pinus taeda* L.) increment cores using a microscopy-based imaging instrument that was designed and fabricated in-house. Detailed here are all aspects of the process/system developed, including the sample preparation, hardware, software, and image processing algorithms. The algorithms were developed in Python (Van Rossum 2007), and most of the operations carried out under the Open Computer Vision Library (OpenCV; Bradski & Kaehler 2008), both of which are open source. We envision this paper being a valuable resource to researchers interested in developing their own in-house capabilities for quantifying resin canal size and frequency for increment cores. The need for such an instrument in our laboratory was driven by a study to investigate tree mortality issues occurring in planted loblolly pine stands growing in the southeastern United States near the "fall line" of Georgia and Alabama; the fall line is the divider between the Piedmont and the Upper Coastal Plain physiographic regions (Eckhardt *et al.* 2010; Ryu *et al.* 2013). It is important to note that loblolly pine is the most important and widely planted among the various southern pine species (Wear & Greis 2012). The exact reasons for the mortality are not known (Coyle *et al.* 2015); however, the possible relationships between tree mortality and the role of resin canals in tree defenses warranted investigation. To assess whether tree mortality could be associated with resin canal properties necessitated the development of a means to efficiently conduct resin canal measurements on a relatively large sampling of wood cores.

Materials and methods

Sampling and pith-to-bark sample preparation

The increment cores used in our process/system development work came from 210 trees sampled from 14 planted loblolly pine stands, all located in Georgia. From each tree, two 12 mm diameter bark-to-bark cores were collected at breast height (1.37 m) using an increment borer; these were placed in individually labeled plastic bags, transported to the laboratory, and stored in a freezer until needed. Each bark-to-bark core was split at the pith to yield two pith-to-bark samples (radial samples), with one processed for the current work and the other kept as a backup. After removing any adhering bark, the samples were dehydrated by soaking in 100% ethanol for three weeks with the ethanol changed once per week (Downes *et al.* 1997); this alternative drying method was employed to reduce cracking due to wood shrinkage that can occur during the drying process. The samples were then soaked in acetone for one week to further remove resinous extractives (Eberhardt & Samuelson 2015). After solvent evaporation and equalizing to laboratory conditions, the samples were glued in between two wood core holders sawn from yellow poplar (*Liriodendron tulipifera* L.) lumber. The dry assemblies were then cut using a twin-blade saw to yield a radial strip with a constant width (2.3 mm tangential dimension) comprised of the remaining increment core wood bordered by adhering strips of wood from the core holders. Another cut with a single blade saw gave a flat transverse surface to the radial strip, now having a constant height (17 mm longitudinal of which 10 mm was core holder and 7 mm was sample). All samples afforded from this process were conditioned at approximately 22°C and 52% relative humidity to achieve a constant moisture content of ~10% before X-ray densitometry.

Annual ring and specific gravity determinations

Delineation of the growth rings in an increment core is needed to assign the resin canals to the specific annual ring in which they are present. The samples were scanned on a QTRS-01X Tree Ring Scanner (Quintek Measurement

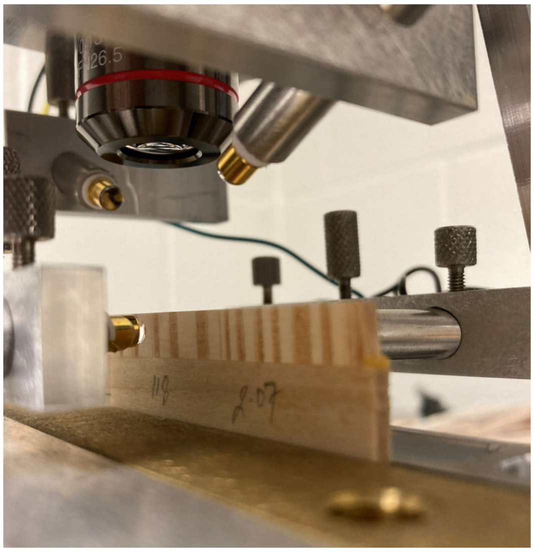

Fig. 1. Imaging setup with 4× objective lens and side 850 nm transmitted lights (top reflected lights not used in this study).

Systems, Knoxville, TN, USA) using a 0.04 mm radial step resolution and the X-ray beam passing through the sample on the radial face. The values measured by the instrument were calibrated to basic specific gravity (SG), that being on an oven-dry weight and green volume basis. Latewood was differentiated from earlywood based on a threshold SG value of 0.48 (Antony *et al.* 2012; Eberhardt & Samuelson 2015). Ring counts determined with said 0.48 threshold were manually checked for accuracy.

Surface preparation for imaging

Resin canal imaging requires even polishing of the transverse surface along the length of each pith-to-bark radial strip. This was accomplished by sanding the transverse surface with a custom-built pneumatic polishing unit we designed and fabricated for this purpose. Aluminum oxide sandpapers (400 and then 600 grit) were used for sanding. The use of silicon carbide sandpaper is not advised since early efforts showed that they left grit on the surface that later interfered with image processing. The samples were sanded until the tracheid walls and lumens were clearly visible; this required approximately eight strokes on each grit of sandpaper.

Imaging system: hardware

The automated microscopy-based imaging system was designed by adapting the capabilities found on the SilviScan (Evans 1994) and the Ring Profiler (Vahey *et al.* 2007) systems. Our custom-built instrument (Fig. 1) provides illumination through the radial surfaces of the sample using six infrared light emitting diodes (LED) at an 850 nm wavelength (LED851L, Thorlabs, Newton, NJ, USA). Thus, light is transmitted through the sample to the polished transverse surface and not supplied from reflected light from the LED lights above. Using this innovative illumination strategy, Evans (1994) found that wood sanding dust in the lumens (for both tracheids and resin canals) appears dark and the tracheid cell walls appear bright.

Because we used infrared light (>700 nm), an important requirement for the imaging system is the transmittance of wavelengths extending beyond the visible range. The imaging system utilizes Olympus parts (Olympus, Tokyo, Japan) including a Plan Fluorite 4× objective lens (UPLFLN 4X) with wavelength range from 380 to 900 nm. The objective is threaded onto a custom-made metal adapter (alternatively one could use Olympus parts) which connects to a tube lens with 22 mm field of view, a 1× camera coupler, and C-mount adapter. An Allied Vision G-235 (Allied

Vision, Stadtroda, Germany) monochrome camera with sensor size of 21.2 mm and resolution of 1936 × 1216 pixels is connected to the microscope system. This particular camera was selected because it has relatively large pixels (5.86 µm) which affords it a relatively high saturation capacity and dynamic range, and it also has suitable sensitivity in the wavelength range of interest. Note that color (RGB) cameras have an infrared filter and thus would not work for this application involving infrared light.

Focusing and pith-to-bark movement were performed using two linear translation stages (x-axis and z-axis), controlled by stepper motors and stepper motor drivers. The initial height of the sample is detected using a U-shaped laser sensor. The samples are then moved under the camera to perform focusing and imaging. The hardware is controlled using an Arduino (Arduino, Somerville, MA, USA) with a 24V Industrial I/O Shield (Rugged Circuits, Wayland, MI, USA).

Software to control image collection

The instrument is connected to a computer using a graphic user interface (GUI) programmed in Python and the tkinter library (Python Software Foundation, https://www.python.org/). Communication between Arduino and Python was done using serial commands. The camera control was done using the pymba library (https://github.com/morefigs/pymba). Most aspects of the image collection were automated through the GUI, except for manually entering the sample name and the length of the sample.

The contrast of the images was adjusted automatically. For each measurement point, a sample image was collected, and the maximum pixel intensity was calculated. The exposure time was then adjusted to have the maximum pixel intensity between 230 and 240. These values provided an image that was sufficiently bright but not saturated in any area. The focus of each image was adjusted by moving the sample along the z-axis. For each measurement point, the Laplacian operator (Pech-Pacheco *et al.* 2000) was used to differentiate between blurry and out-of-focus images. The Laplacian operator finds the edges within an image, and the more edges found indicates images that are more in focus. These two operations (contrast adjustment and focus) were done for every measurement point. Only the in-focus and contrast-optimal images were saved by the GUI. The process of adjusting the focus and the contrast was done for each image collected along the pith-to-bark radial sample.

The images from each sample were saved into their own unique folder, and the images were labeled in sequence, starting from the pith end of the sample, and progressing to the bark end of the sample. The images were saved as greyscale images with 8-bit depth. The 210 pith-to-bark radial samples yielded 24 153 images that contained overlapping information. Image processing was done offline and not during image collection.

Image processing

The images were processed using Python version 3.7 (Van Rossum 2007) in the Spyder integrated development environment (IDE; Raybaut 2009) using OpenCV (Bradski & Kaehler 2008), NumPy (Oliphant 2006) and pandas (McKinney 2011) libraries. The camera was calibrated using a microscope stage calibration slide of 1 mm total length (AmScope, Irvine, CA, USA) (Bradski & Kaehler 2008). The calibration resulted in 1 mm of length being equal to 623 pixels. Based on the camera calibration and the sensor size of 1216 pixels, the tangential width imaged was 1.95 mm, and each pixel represented 1.6 µm.

The first and last images were manually cropped to the start and end of each sample. Each image was then cropped in the radial direction to keep the central portion of the images as they were clearer than the edges of the images; the tangential image width was not cropped and thus the area imaged was equal to the width of the camera sensor (1216 pixels). Except for the first and last images, the center portion of each image was cropped starting from 668 to 1336 pixels from the original 1936 pixels width of the image. The first images were cropped to provide any information from the sample's start to the 668th pixel of the 2nd image. The last image was cropped from the 668th pixel to the end of the sample.

A series of image operations were done to improve the image quality prior to resin canal identification. The contrast of the image was adjusted by using the contrast limited adaptive histogram equalization (CLAHE) algorithm of tiles size 14 × 14 pixels (Pizer *et al.* 1990; Sasi & Jayasree 2013). Noise removal was then done by using the non-local means denoising algorithm using a template window size of 7 and a search window size of 21 pixels (Buades *et al.* 2011; Zhang 2022). The images were then converted into binary images by applying the gaussian adaptive threshold algorithm (Yan *et al.* 2005) and then inverted to yield a binary image with the cell walls being dark (pixel value = 0) and the lumens being bright (pixel value = 255). To separate resin canals from any tracheid lumens and the rays, morphological operations were then done on the inverted images. First, the bright lumens were eroded using a kernel size of 25 × 25 pixels. The contours were then found by using hierarchical contour retrieval models (Arbelaez *et al.* 2010). The smaller contours of the tracheid lumens, having an area of 800 pixels or less, were removed. The remaining contours were then dilated using a kernel size of 25 × 25 pixels to restore them to their original size. To separate the rays from the resin canals, the aspect ratio of the remaining contours was calculated and objects with a ratio of the height to the width of more than 2 (rays) were converted to 0. The rays touching the resin canals were then isolated by erosion using a kernel size of 15 × 1 pixels and then the resin canals were dilated using the same kernel size.

The contrast-fixed and noise removed image, the binary image containing the resin canals as white and the rest black, and the weighted image which is a combination of the first two images were saved together as a three-channel image. There were some errors in the resin canals delineation process, particularly near the pith; these errors were fixed manually, whereby missing resin canals were added, and any areas that were labeled incorrectly as resin canals were deleted.

Extracting resin canal information

To extract the resin canals from pith to bark in each sample, the binary images were horizontally concatenated and then the contours of the concatenated image were found. From each contour, the radius, area, perimeter, coordinates for the centroid, maximum and minimum points were all calculated using image moments (Teague 1980; Rocha *et al.* 2002). The extracted information thus contained the resin canal area in pixels and coordinates (centroid, minimum, maximum) for the *x*-axis and *y*-axis for each resin canal. The resin canal information was exported to a comma-separated values (CSV) file.

Merging resin canal data with X-ray densitometry data

After completing the image analysis in Python, we used R (R Core Team 2024) and RStudio (RStudio Team 2024) interface for all further steps. The resin canal information was aligned with X-ray densitometry data to assign each resin canal to each annual ring and whether the resin canal was found within the earlywood and latewood. This alignment was done using the normalized cross-correlation method (Keane & Adrian 1992; Yoo & Han 2009). To facilitate comparison between 2 different signal types, a pseudo-SG value was calculated from the contrast corrected and noise removed images. This was accomplished by averaging the pixel values in the images in the tangential direction for each radial position. Because each image pixel represents a higher resolution (0.0015 mm) than each X-ray data point (0.04 mm), the image data were averaged into 0.04 mm increments in the radial direction. Both the SG and the image data were then normalized by:

$$Z = \frac{X - \mu}{\sigma} \qquad (1)$$

where Z is the normalized pseudo-SG value (ranging from 0 to 1), X is the mean pixel/SG value, μ is the overall mean and σ is standard deviation. The normalized values from the images and the X-ray densitometer were then aligned using the normalized cross-correlation method (Keane & Adrian 1992; Yoo & Han 2009). The image was shifted from left to right and the highest cross correlation value was found. A plot for each sample was then constructed with

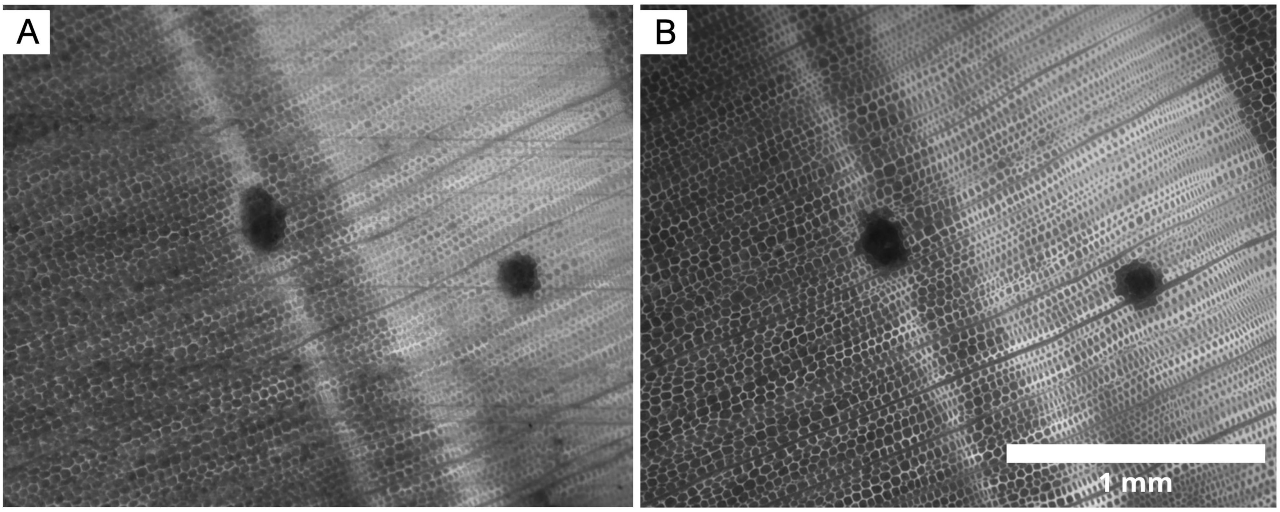

Fig. 2. Image of resin canals of loblolly pine after sanding with 400 grit sandpaper (A) and 600 grit sandpaper (B).

the normalized values overlaid onto each other to confirm the image data was accurately matched with the X-ray densitometry data.

The resin canal data were then merged with the annual ring information. The resin canals were assigned to either earlywood or latewood based on the 0.48 threshold and then manually checked for accuracy. Ring level resin canal information was then calculated which included the resin canal number, area, average size (area divided by number), and resin canal percent (resin canal area divided by sample area of each annual ring); the same information was found for the earlywood and latewood proportion of each annual ring. Any resin canal not fully in frame was counted as a half resin canal if its area was less than the median resin canal size for those that were fully in frame (not touching top or bottom edge).

Results and discussion

The automated microscopy-based imaging system produced high-quality images (Fig. 2) from the bark-to-pith samples with one exception, images collected for the growth rings near the pith where significant variation in the image quality seemed to occur; this was attributed to this part of the sample being less amenable to polishing. Specifically, the first 2–3 images at the pith were less clear, with visible scratches, and generally poor contrast with the cell walls being not very bright. We found that the material near the pith was removed quickly while polishing because of the soft and spongy nature of both the pith itself and the wood near the pith.

The developed algorithms worked well for most images, the exception being the poor-quality images collected near the pith as noted above, and some of the images with empty resin duct lumens (without wood sanding dust, so illuminated as white) (Figs 3 and 4). The images at the pith also had low contrast owing to the poor light transmission from the pith itself and the particularly thin-walled tracheids found in the first few growth rings (Chen *et al.* 2008). As such, the regions near the pith required more manual correction than the images collected at older cambial ages.

Figure 5 shows a portion of the normalized pseudo-SG data for one sample, derived both from the images and the X-ray densitometry data. The unaligned pseudo-SG profiles are shown in the top figure; the pseudo-SG profiles after alignment via optimized cross-correlation are shown at the bottom. For all samples the procedure was effective at aligning the image within the X-ray densitometry data and no manual corrections were needed. This algorithm allowed us to assign resin canals accurately into cambial age (ring number) to match our X-ray densitometry data.

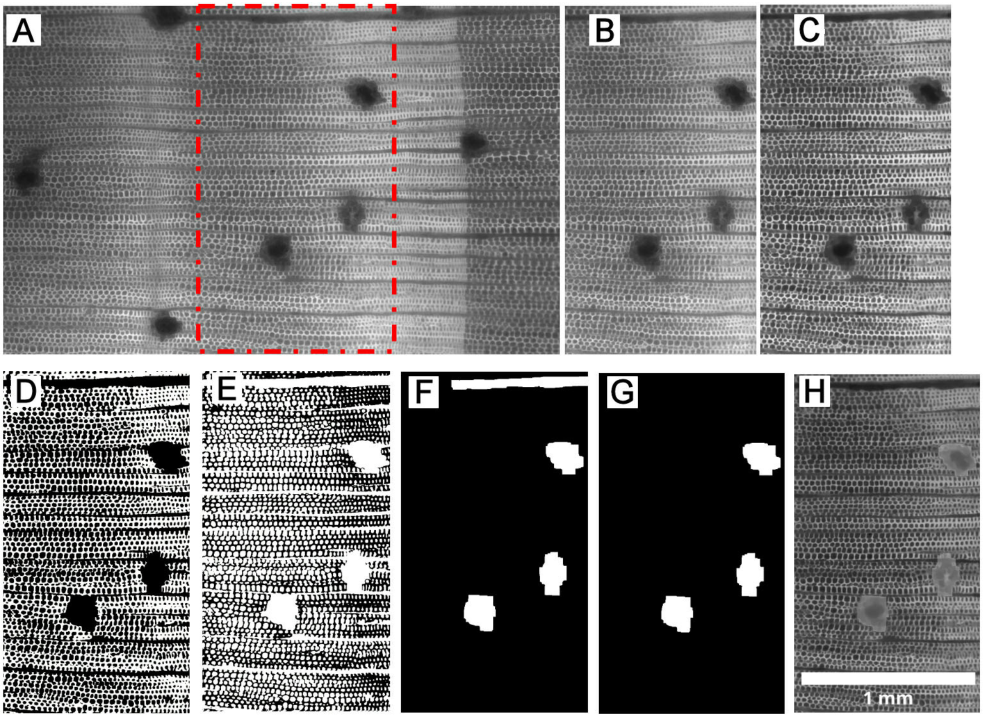

Fig. 3. Example of the sequence of image processing techniques of resin canals of loblolly pine: (A) Image before cropping, (B) image after cropping; red dotted line indicates the cropped portion of the image, (C) contrast corrected and noise removed image, (D) image after applying the binary threshold, (E) inverted image, (F) isolated resin canals and rays, (G) image after ray removed using an aspect ratio of contours, (H) weighted image where the image is merged with the identified resin canals.

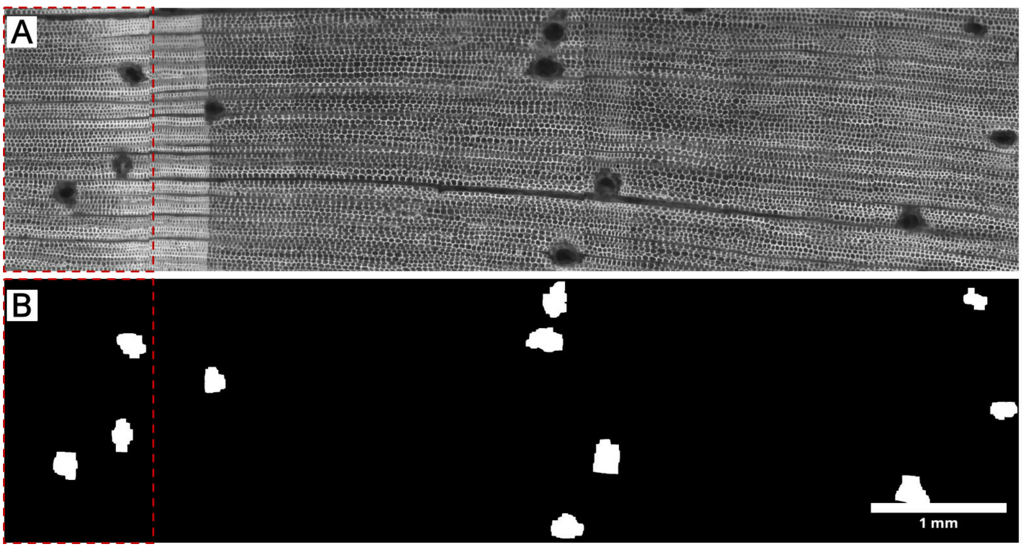

Fig. 4. Example of the image concatenations: (A) Image subsamples showing seven concatenated images, (B) image showing isolated, and now quantifiable, resin canals for the seven concatenated images in loblolly pine.

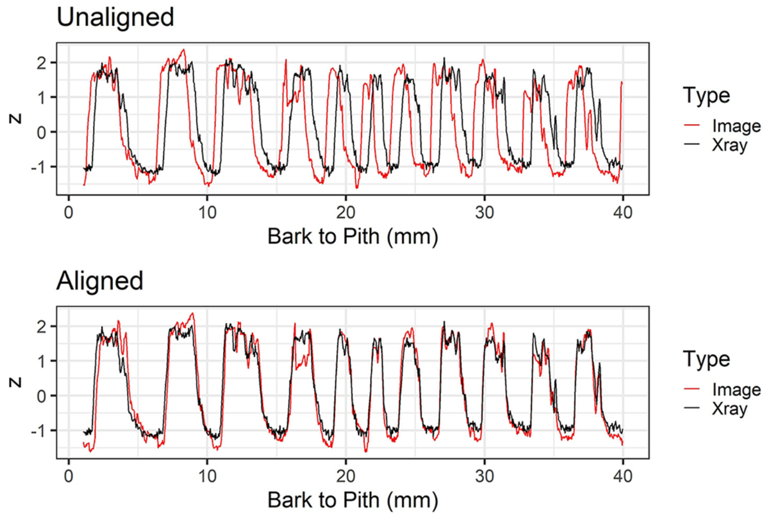

Fig. 5. A subset of normalized data from an increment core sample showing unaligned (top) and aligned (bottom) signals based on image pixel and pseudo-SG (X-ray) values, respectively.

Table 1. Resin canal summary within the area imaged and separated into resin canals found in earlywood versus latewood for various ring number ranges of loblolly pines.

Ring number ranges (years)	Growth ring zones	Resin canals			
		Number observed (N)	Percentage per zone (%)	Total area in each zone (mm^2)	Average size (mm^2)
All	Earlywood	12 603	51.5	334.4	0.0265
	Latewood	11 888	48.5	404.8	0.0340
	Both	24 491		739.2	0.0302
1-6	Earlywood	9389	74.3	216.9	0.0231
	Latewood	3241	25.6	96.3	0.0297
	Both	12 630		313.2	0.0248
7+	Earlywood	3214	27.1	117.5	0.0366
	Latewood	8647	72.9	308.6	0.0357
	Both	11 861		426.1	0.0359

A total of 24 491 resin canals were identified in the pith-to-bark concatenated images of the increment cores from 210 trees; these resin canals had a total area of 739.2 mm^2 (Table 1). Of the total number of resin canals identified, slightly more than half of them (51.5%) were found in the earlywood. This result is in contrast with literature for other conifer species. For instance, Reid & Watson (1966) found that 80% of the resin canals in Ponderosa pine (*Pinus contorta* Dougl.) are located within the later 40% of the growth ring. Wimmer *et al.* (1999) and Cown *et al.* (2011) both report a common occurrence of resin canals between the earlywood and latewood transition in Radiata pine (*Pinus radiata* D.) and Norway Spruce (*Picea abies* L.). For loblolly pine, Blanche *et al.* (1992) observed an increase in resin canal frequency from 3 per square cm to 44 per square cm from the early to late growing season. Figure 6 shows unimodal distributions of resin canal areas found in the earlywood and the latewood for all resin canals identified. While the number of resin canals was quite similar between the earlywood and the latewood, the resin canal size distributions show that for our loblolly pine trees, the individual sizes of the resin canals were larger in the latewood.

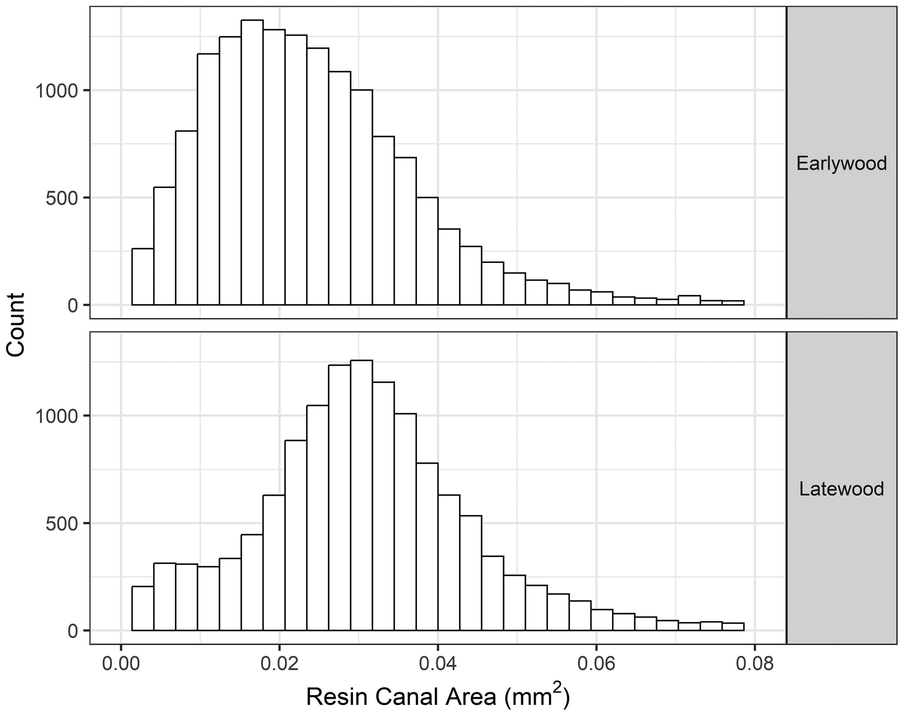

Fig. 6. Histogram size classes of individual resin canal areas determined for earlywood (top) and latewood (bottom) growth ring zones in loblolly pine.

As a preliminary assessment of our findings, we examined annual variation of resin canals within the earlywood and latewood and found that there were more earlywood resin canals in years 1 to 6 (ring numbers), and from 7 and above there were more resin canals found in the latewood. After ring 6, the latewood resin canals were much more numerous than the earlywood resin canals, although their size was similar. These results generally match the findings by Yang *et al.* (2006) and Chen *et al.* (2008) who found that resin canals are smaller in dimension and more randomly distributed near the pith. Figure 7 shows the relative within-ring distribution of the resin canals for annual rings 1 to 6 years and for 7+ years; the relative position, starting at the onset of earlywood formation, was calculated by dividing each ring position increment by the total ring width. For years 1 to 6, the average latewood percentage was 20%, and resin canals were found to be fairly uniform on either side of the earlywood-to-latewood boundary. For years 7 and greater, the average latewood percentage was 50%, and resin canals were mostly concentrated within the latewood next to the earlywood-to-latewood boundary. Note that the position and distribution of resin canal within annual rings is generally thought to be a function of numerous factors including drought, temperature, pressure, wind, photoperiod, and available growth substances (Bailey & Faull 1934; Fahn & Zamski 1970; Fahn *et al.* 1979; Wimmer & Grabner 1997; Cown *et al.* 2004). In the present report, it is beyond the scope to assess relationships between the resin canal quantifications and the health and vigor of the study trees; however, with the data provided, it is clearly demonstrated that the imaging system developed in our laboratory is a powerful tool to gather detailed information from a large sampling of increment cores.

Limited literature exists on loblolly pine regarding the distribution of resin canals across annual rings. For other conifer species, some of the available literature divides the distribution of resin canals into three zones; earlywood, earlywood-to-latewood transition, and latewood (Cown *et al.* 2011). Despite the detailed information that can be gleaned from our imaging system, classifying resin canals into the earlywood-to-latewood transition is inherently problematic because any such separation depends upon the definition for latewood selected (Koubaa *et al.* 2002;

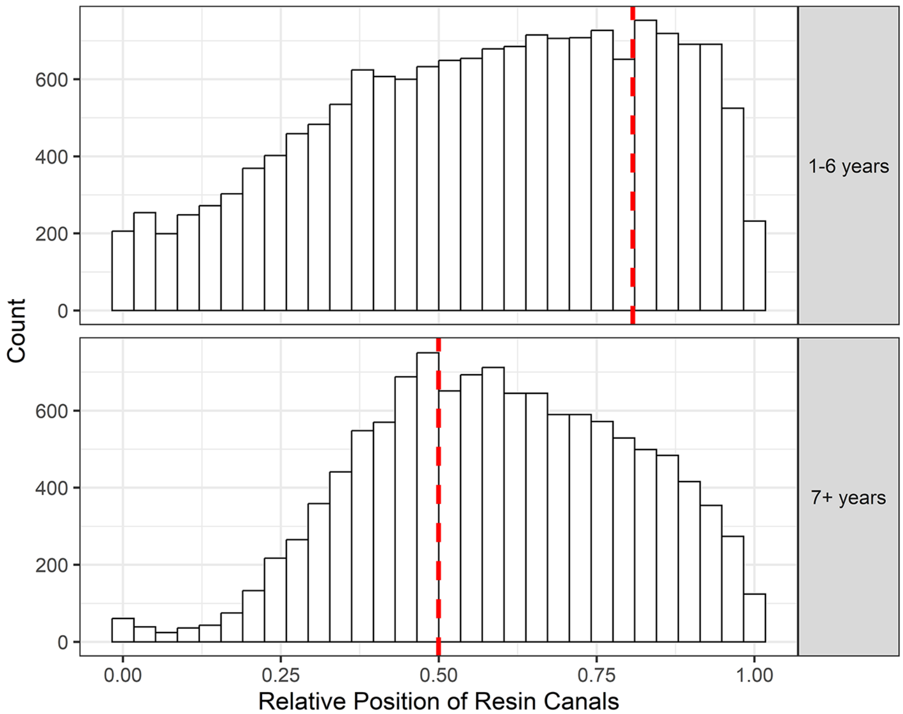

Fig. 7. The relative position of resin canals within annual rings separated into two ring number groups: years 1–6 years (top) and years 7+ (bottom) in loblolly pine. The vertical red lines indicate the relative position within the ring separating earlywood and latewood using a 0.480 specific gravity threshold.

Eberhardt & Samuelson 2015; Cartenì *et al.* 2018). Handling anomalies such as false rings are also problematic. Loblolly pine typically has a distinct earlywood-to-latewood transition which allowed us to separate the two using a threshold SG value (0.48) (Eberhardt & Samuelson 2015; Dahlen *et al.* 2018, 2023); we then visually verified the classification. For species with a gradual transition from earlywood to latewood, classification would be more difficult.

It is acknowledged that the quantification of resin canals, as well as other wood anatomical features, can be achieved through other means, with the most traditional being the use of a microscope with thin sections prepared using a microtome (LaPasha & Wheller 1990). Flatbed scanners are relatively inexpensive for their resolution (2400 dpi) and they have been widely adopted in the dendrochronology field for ring counting, although others have used them for studies on resin canals (Chen *et al.* 2008; Thomas & Collins 2017). Because of the relatively limited resolving power of scanners, whereby scanning at 2400 dpi would provide a theoretical pixel size of 10.6 µm (resolving details at this resolution is likely not feasible) versus the 1.6 µm pixel size here, smaller resin canals and resin canals in the earlywood can be difficult to detect. Griffin *et al.* (2021) recently developed dendrochronological techniques coupled with 'gigapixel macro photography', which utilizes a DLSR camera coupled with reflective light and focus stacking to capture tree rings from increment cores at the macroscopic level. This imaging technique provides high-resolution images compared to flatbed scanners at the macro level, and it could be adapted for resin canals, however the reflected light setup means that sample preparation is more critical than the transmitted light setup used here and adapted from Evans (1994). X-ray computed tomography (CT) is another alternative method to measure wood macroscopic and microscopic features. Relative to the methods used here, X-ray CT can provide higher resolution information and information in 3D from tissue to the subcellular level (e.g., cell walls and pits) and does not require sample preparation, however, the hardware setup is astronomically more expensive, and slower than what we used here (Van den Bulcke *et al.* 2019).

We intend to continue to develop the hardware and software used here with the intent to extract more anatomical features in the future such as the diameters of the tracheids. Evans (1994) combined image data with X-ray densitometry data to infer cell wall thickness and fiber coarseness. We routinely use X-ray densitometry to measure annual ring, earlywood, and latewood width and SG (Dahlen *et al.* 2018; Dahlen *et al.* 2023), and herein demonstrate the ability to align the density profile to the annual rings imaged, thus with further development we anticipate our system will also have the capacity to measure tracheid anatomical features. Extracting tracheid diameters will likely require polishing samples with higher grit sandpaper than used here (600-grit) (Evans 1994; Schimleck *et al.* 2019). We anticipate a number of software improvements could be implemented in the future to improve image quality prior to extracting features from the images as follows: (1) multiple frames averaged together may increase the signal-to-noise ratio by reducing the random electronic noise; (2) by combining different exposures together to further reduce noise and increase dynamic range (Robertson *et al.* 1999), different focal lengths may be combined to create an image that is more in focus using the scale-invariant feature transform algorithm (Lowe 2004) which was recently implemented in OpenCV (Bradski & Kaehler 2008). Finally, this study captured 8-bit images that contain values from 0 (dark) to 255 (bright) for each pixel; we intend to explore the improvement that higher bit (e.g. 12-bit) images would provide (Klette 2014). We also intend to concatenate the images via stitching instead of the method used here, although this will be done outside of the OpenCV library since that implementation is designed for panorama images (Bradski & Kaehler 2008). Here, the separation of resin canals from other cell types were isolated using traditional image processing techniques, we intend to explore deep and machine learning techniques in future studies using this data for training the models.

Conclusion

This paper describes the hardware, software, image processing and data analysis techniques used here to image radial wood samples from pith to bark to measure resin canal information. To our knowledge, this represents the largest study quantifying resin canal information in loblolly pine. A custom-built imaging system was built and was proven to be an effective instrument for capturing images on large scales. The use of near-infrared light to illuminate a sanded samples' surface helps to separate resin canals from surrounding features. The semi-automated program facilitated rapid image processing, resin canal delineation and quantification.

Acknowledgements

The work was supported by the USDA Forest Service, Forest Products Laboratory (No. 16-JV-11111134-060), the University of Georgia (No. 10-21-RX064-663) and NIFA McIntire-Stennis (No. 1023340). The utmost gratitude is extended to C. Tim Scott for sharing a Ring Profiler prototype concept he developed and for invaluable discussions about image processing for the images gathered via an innovative approach to sample illumination. We thank Rob Evans for providing information regarding his experience with the SilviScan system, including discussing the effect of different wavelength LED lights for imaging. We thank Geoff Downes for providing his experience with polishing samples for the SilviScan system.

References

Antony F, Schimleck LR, Daniels RF. 2012. A comparison of earlywood–latewood demarcation methods–a case study in loblolly pine. *IAWA J.* 33: 187–195. DOI: 10.1163/22941932-90000088.

Arbelaez P, Maire M, Fowlkes C, Malik J. 2010. Contour detection and hierarchical image segmentation. *IEEE Trans. Pattern Anal. Machine Intell.* 33: 898–916. DOI: 10.1109/TPAMI.2010.161.

Arbellay E, Stoffel M, Sutherland EK, Smith KT, Falk DA. 2014. Resin duct size and density as ecophysiological traits in fire scars of *Pseudotsuga menziesii* and *Larix occidentalis*. *Ann. Bot.* 114: 973–980. DOI: 10.1093/aob/mcu168.

Bailey IW, Faull AF. 1934. The cambium and its derivative tissues: no. IX. Structural variability in the redwood, *Sequoia sempervirens*, and its significance in the identification of fossil woods. *J. Arnold Arbor.* 15: 233–254.

Beleko S. 2021. Pine resin productivity at Sao Hill forest plantation, Southern Tanzania. *Tanz. J. For. Nat. Conserv.* 90: 82–95.

Blanche CA, Lorio Jr PL, Sommers RA, Hodges JD, Nebeker TE. 1992. Seasonal cambial growth and development of loblolly pine: xylem formation, inner bark chemistry, resin ducts, and resin flow. *For. Ecol. Manage.* 49: 151–165. DOI: 10.1016/0378-1127(92)90167-8.

Bollschweiler M, Stoffel M, Schneuwly DM, Bourqui K. 2008. Traumatic resin ducts in *Larix decidua* stems impacted by debris flows. *Tree Physiol.* 28: 255–263. DOI: 10.1093/treephys/28.2.255.

Bosshard HH, Hug UE. 1980. Die Anastomosen im Harzkanalsystem von *Picea abies* (L.) Karst., *Larix decidua* Mill. und *Pinus sylvestris* L. *Holz Roh Werkst.* 38: 325–328. DOI: 10.1007/BF02611082.

Bradski G, Kaehler A. 2008. *Learning OpenCV: Computer vision with the OpenCV library*. O'Reilly Media, Newton, MA.

Buades A, Coll B, Morel J-M. 2011. Non-local means denoising. *Image Process. Online* 1: 208–212. DOI: 10.5201/ipol.2011.bcm_nlm.

Cabrita P. 2018. Resin flow in conifers. *J. Theor. Biol.* 453: 48–57. DOI: 10.1016/j.jtbi.2018.05.020.

Cabrita P. 2021. A model for resin flow. In: Ramawat KG, Ekiert HM, Goyal S (eds.), *Plant Cell and Tissue Differentiation and Secondary Metabolites: Fundamentals and Applications*: 117–144. Springer, Cham. DOI: 10.1007/978-3-030-30185-9_5.

Cartenì F, Deslauriers A, Rossi S, Morin H, De Micco V, Mazzoleni S, Giannino F. 2018. The physiological mechanisms behind the earlywood-to-latewood transition: a process-based modeling approach. *Front. Plant Sci.* 9: 354696. DOI: 10.3389/fpls.2018.01053.

Catherwood AA, Knapp PA, Mitchell TJ. 2022. Scientific Note: Loblolly pine traumatic resin ducts serve as indicators of cool-season weather events at Nags Head, North Carolina. *Castanea* 86: 296–304. DOI: 10.2179/0008-7475.86.2.296.

Chauhan K, Sharma KR, Dutt B, Chauhan R. 2022. Comparative anatomy of resin ducts in some Western Himalayan softwoods. *Vegetos* 35: 935–941. DOI: 10.1007/s42535-022-00375-6.

Chen F, Evans R. 2005. A robust approach for vessel identification and quantification in eucalypt pulpwoods. *Appita* 58: 442–447. DOI: 10.3316/informit.570037896915278.

Chen FF, Evans R. 2010. Automated measurement of vessel properties in birch and poplar wood. *Holzforschung* 64: 369–374. DOI: 10.1515/hf.2010.057.

Chen FF, Yang JL, Downes G. 2008. A visual information assessment tool for resin canal identification and property measurement. *IAWA J.* 29: 397–408. DOI: 10.1163/22941932-90000194.

Cown DJ, Donaldson LA, Downes GM. 2011. A review of resin features in radiata pine. *New Zeal. J. For.* 1: 41–60.

Cown DJ, Downes GM, Donaldson LA. 2004. *Sources of variation in resin ducts – literature review*. WQI Report APP 36. WQI, Poole.

Coyle DR, Klepzig KD, Koch FH, Morris LA, Nowak JT, Oak SW, Otrosina WJ, Smith WD, Gandhi KJK. 2015. A review of southern pine decline in North America. *For. Ecol. Manage.* 349: 134–148. DOI: 10.1016/j.foreco.2015.04.007.

Dahlen J, Auty D, Eberhardt TL. 2018. Models for predicting specific gravity and ring width for loblolly pine from intensively managed plantations, and implications for wood utilization. *Forests* 9: 292. DOI: 10.3390/f9060292.

Dahlen J, Auty D, Eberhardt TL, Schimleck L, Pokhrel NR. 2023. Determination of ring-level dynamic modulus of elasticity in loblolly pine from measurements of ultrasonic velocity and specific gravity. *Forestry* 96: 588–604. DOI: 10.1093/forestry/cpac063.

DeRose RJ, Bekker MF, Long JN. 2017. Traumatic resin ducts as indicators of bark beetle outbreaks. *Can. J. For. Res.* 47: 1168–1174. DOI: 10.1139/cjfr-2017-0097.

Downes GM, Hudson IL, Raymond CA, Dean GH, Michell AJ, Schimleck LR, Evans R, Muneri A. 1997. *Sampling plantation eucalypts for wood and fibre properties*. CSIRO Publishing, Melbourne, VIC.

Eberhardt TL, Samuelson LJ. 2015. Collection of wood quality data by X-ray densitometry: a case study with three southern pines. *Wood Sci. Technol.* 49: 739–753. DOI: 10.1007/s00226-015-0732-x.

Eckhardt L, Sword Sayer MA, Imm D. 2010. State of pine decline in the southeastern United States. *South. J. Appl. For.* 34: 138–141.

Evans R. 1994. Rapid measurement of the transverse dimensions of tracheids in radial wood sections from *Pinus radiata*. *Holzforschung* 48: 168–172. DOI: 10.1515/hfsg.1994.48.2.168.

Evert RF. 2006. *Esau's plant anatomy: meristems, cells, and tissues of the plant body: their structure, function, and development*. Wiley, Chichester.

Fabián-Plesníková I, Sáenz-Romero C, Cruz-De-León J, Martínez-Trujillo M, Sánchez-Vargas NM, Terrazas T. 2021. Heritability and characteristics of resin ducts in *Pinus oocarpa* stems in Michoacán, Mexico. *IAWA J.* 42: 258–278. DOI: 10.1163/22941932-bja10055.

Fahn A, Zamski E. 1970. The influence of pressure, wind, wounding and growth substances on the rate of resin duct formation in *Pinus halepensis* wood. *Isr. J. Bot.* 19: 429–446.

Fahn A, Werker E, Ben-Tzur P. 1979. Seasonal effects of wounding and growth substances on development of traumatic resin ducts in *Cedrus libani*. *New Phytol.* 82: 537–544. DOI: 10.1111/j.1469-8137.1979.tb02680.x.

Gärtner H, Cherubini P, Fonti P, von Arx G, Schneider L, Nievergelt D, Verstege A, Bast A, Schweingruber FH, Büntgen U. 2015. A technical perspective in modern tree-ring research-how to overcome dendroecological and wood anatomical challenges. *JoVE* 97: e52337. DOI: 10.3791/52337.

Griffin D, Porter ST, Trumper ML, Carlson KE, Crawford DJ, Schwalen D, McFadden CH. 2021. Gigapixel macro photography of tree rings. *Tree-Ring Res.* 77: 86–94. DOI: 10.3959/TRR2021-3.

Guillén L, Adaime R, Birke A, Velázquez O, Angeles G, Ortega F, Ruíz E, Aluja M. 2017. Effect of resin ducts and sap content on infestation and development of immature stages of *Anastrepha obliqua* and *Anastrepha ludens* (Diptera: Tephritidae) in four mango (Sapindales: Anacardiaceae) cultivars. *J. Econ. Entomol.* 110: 719–730. DOI: 10.1093/jee/tow279.

Hood S, Sala A. 2015. Ponderosa pine resin defenses and growth: metrics matter. *Tree Physiol.* 35: 1223–1235. DOI: 10.1093/treephys/tpv098.

Hood SM, Reed CC, Kane JM. 2020. Axial resin duct quantification in tree rings: A functional defense trait. *MethodsX.* 7: 101035. DOI: 10.1016/j.mex.2020.101035.

Kane JM, Kolb TE. 2010. Importance of resin ducts in reducing ponderosa pine mortality from bark beetle attack. *Oecologia* 164: 601–609. DOI: 10.1007/s00442-010-1683-4.

Keane RD, Adrian RJ. 1992. Theory of cross-correlation analysis of PIV images. *Appl. Sci. Res.* 49: 191–215.

Kibblewhite RP, Thompson NS. 1973. The ultrastructure of the middle lamella region in resin canal tissue isolated from slash pine holocellulose. *Wood Sci. Technol.* 7: 112–126. DOI: 10.1007/BF00351154.

Klette R. 2014. *Concise computer vision*. Springer, London.

Knebel L, Robison DJ, Wentworth TR, Klepzig KD. 2008. Resin flow responses to fertilization, wounding and fungal inoculation in loblolly pine (*Pinus taeda*) in North Carolina. *Tree Physiol.* 28: 847–853. DOI: 10.1093/treephys/28.6.847.

Koch P. 1972. Utilization of the southern pines. Vols. 1 and 2. Agriculture Handbook No. 420 US Southern Forest Experiment Station, Asheville, NC.

Koubaa A, Zhang SYT, Makni S. 2002. Defining the transition from earlywood to latewood in black spruce based on intra-ring wood density profiles from X-ray densitometry. *Ann. For. Sci.* 59: 511–518. DOI: 10.1051/forest:2002035.

Krokene P, Nagy NE, Krekling T. 2008. Traumatic resin ducts and polyphenolic parenchyma cells in conifers. In: Schaller A (ed.), *Induced Plant Resistance to Herbivory*: 147–169. Springer, Dordrecht. DOI: 10.1007/978-1-4020-8182-8_7.

Krokene P, Nagy NE. 2012. Anatomical aspects of resin-based defenses in pine. In: Fett-Neto AG (ed.), *Pine resin: biology, chemistry and applications*: 67–86. Research Signpost, Thiruvananthapuram.

LaPasha CA, Wheeler EA. 1990. Resin canals in *Pinus taeda*: longitudinal canal lengths and interconnections between longitudinal and radial canals. *IAWA J.* 11: 227–238. DOI: 10.1163/22941932-90001180.

Larson PR. 1994. *The vascular cambium, development and structure*. Springer, Berlin.

Levkoev E, Kilpeläinen A, Luostarinen K, Pulkkinen P, Mehtätalo L, Ikonen V-P, Jaatinen R, Zhigunov A, Kangas J, Peltola H. 2017. Differences in growth and wood density in clones and provenance hybrid clones of Norway spruce. *Can. J. For. Res.* 47: 389–399. DOI: 10.1139/cjfr-2016-0285.

Lombardero MJ, Ayres MP, Lorio Jr PL, Ruel JJ. 2000. Environmental effects on constitutive and inducible resin defenses of *Pinus taeda*. *Ecol. Lett.* 3: 329–339. DOI: 10.1046/j.1461-0248.2000.00163.x.

Lowe DG. 2004. Distinctive image features from scale-invariant keypoints. *Int. J. Comput. Vision* 60: 91–110. DOI: 10.1023/B:VISI.0000029664.99615.94.

McKinney W. 2011. pandas: A foundational Python library for data analysis and statistics. *Python for High Performance and Scientific Computing* 14: 1–9.

Neis FA, de Costa F, de Almeida MR, Colling LC, de Oliveira Junkes CF, Fett JP, Fett-Neto AG. 2019. Resin exudation profile, chemical composition, and secretory canal characterization in contrasting yield phenotypes of *Pinus elliottii* Engelm. *Ind. Crops Prod.* 132: 76–83. DOI: 10.1016/j.indcrop.2019.02.013.

Nixon M, Aguado A. 2019. *Feature extraction and image processing for computer vision*. Academic Press, San Diego, CA.

Oliphant TE. 2006. *Guide to numpy*, Vol. 1. Trelgol Publishing.

Pech-Pacheco JL, Cristóbal G, Chamorro-Martinez J, Fernández-Valdivia J. 2000. Diatom autofocusing in brightfield microscopy: a comparative study. In: *Proceedings 15th International Conference on Pattern Recognition. ICPR-2000, Vol. 3*: 314–317. DOI: 10.1109/ICPR.2000.903548.

Pizer SM, Johnston RE, Ericksen JP, Yankaskas BC, Muller KE. 1990. Contrast-limited adaptive histogram equalization: speed and effectiveness. In: *Proceedings of the First Conference on Visualization in Biomedical Computing, Atlanta, GA, USA, 1990*: 337–345. DOI: 10.1109/VBC.1990.109340p.

R Core Team. 2024. *R: A language and environment for statistical computing*. R Foundation for Statistical Computing, Vienna. Available online at https://www.R-project.org/.

Raffa KF. 2014. Terpenes tell different tales at different scales: glimpses into the chemical ecology of conifer-bark beetle-microbial interactions. *J. Chem. Ecol.* 40: 1–20. DOI: 10.1007/s10886-013-0368-y.

Raybaut P. 2009. *Spyder-documentation*. Available online at: pythonhosted.org.

Reid RW, Watson JA. 1966. Sizes, distributions, and numbers of vertical resin ducts in lodgepole pine. *Can. J. Bot.* 44: 519–525. DOI: 10.1139/b66-062.

Richter HG, Grosser D, Heinz I, Gasson PE. 2004. IAWA list of microscopic features for softwood identification. *IAWA J.* 25: 1–70.

Robertson MA, Borman S, Stevenson RL. 1999. Dynamic range improvement through multiple exposures. In: *Proceedings 1999 International Conference on Image Processing* (*Cat. 99CH36348*)*, Kobe, Japan*, *Vol. 3*: 159–163. DOI: 10.1109/ICIP.1999.817091.

Rocha L, Velho L, Carvalho PCP. 2002. Image moments-based structuring and tracking of objects. In: *Proceedings of XV Brazilian Symposium on Computer Graphics and Image Processing*: 99–105. DOI: 10.1109/SIBGRA.2002.1167130.

Rodríguez-García A, López R, Martín JA, Pinillos F, Gil L. 2014. Resin yield in *Pinus pinaster* is related to tree dendrometry, stand density and tapping-induced systemic changes in xylem anatomy. *For. Ecol. Manage.* 313: 47–54. DOI: 10.1016/j.foreco.2013.10.038.

RStudio Team. 2024. *RStudio: Integrated Development for R*. RStudio, Boston, MA. Available online at http://www.rstudio.com.

Ruffinatto F, Negro F, Crivellaro A. 2023. The macroscopic structure of wood. *Forests* 14: 644. DOI: 10.3390/f14030644.

Ryu SR, Wang GG, Walker JL. 2013. The health of loblolly pine stands at Fort Benning, GA. In: Guidin JM (ed.), *The health of loblolly pine stands at Fort Benning, GA* (*SRS-175*): 543–549. U.S. Department of Agriculture, Forest Service, Southern Research Station, Asheville, NC.

Sasi NM, Jayasree VK. 2013. Contrast limited adaptive histogram equalization for qualitative enhancement of myocardial perfusion images. *Engineering* 10: 326–331. DOI: 10.4236/eng.2013.510B066.

Schimleck L, Dahlen J, Apiolaza LA, Downes G, Emms G, Evans R, Moore J, Pâques L, Van den Bulcke J, Wang X. 2019. Non-destructive evaluation techniques and what they tell us about wood property variation. *Forests* 10: 728. DOI: 10.3390/f10090728.

Sjöström E. 1993. *Wood chemistry: fundamentals and applications*. Academic Press, San diego, CA.

Susilowati A, Rachmat HH. 2018. Growth and Resin Production Structure of *Pinus merkusii* Under Different Environment Condition (Case study in Perum perhutani Seedling Seed Orchard). In: *IOP Conference Series: Earth and Environmental Science*, *Vol. 209*. *No. 1*: 012028. IOP Publishing. DOI: 10.1088/1755-1315/209/1/012028.

Teague MR. 1980. Image analysis via the general theory of moments. *J. Opt. Soc. Am.* 70: 920–930. DOI: 10.1364/JOSA.70.000920.

Thomas J, Collings DA. 2017. Detection and mapping of resin canals by image analysis in transverse sections of mechanically perturbed, young *Pinus radiata* trees. *IAWA J.* 38: 170–181. DOI: 10.1163/22941932-20170166.

Vahey DW, Zhu JY, Scott CT. 2007. Wood density and anatomical properties in suppressed-growth trees: Comparison of two methods. *Wood Fiber Sci.* 39: 462–471.

Van den Bulcke J, Boone MA, Dhaene J, Van Loo D, Van Hoorebeke L, Boone MN, Wyffels F, Beeckman H, Van Acker J, De Mil T. 2019. Advanced X-ray CT scanning can boost tree ring research for earth system sciences. *Ann. Bot.* 124: 837–847. DOI: 10.1093/aob/mcz126.

Van Rossum G. 2007. Python Programming Language. In: *USENIX Annual Technical Conference, Vol. 41*: 1–36.

Vázquez-González C, Zas R, Erbilgin N, Ferrenberg S, Rozas V, Sampedro L. 2020. Resin ducts as resistance traits in conifers: linking dendrochronology and resin-based defenses. *Tree Physiol.* 40: 1313–1326. DOI: 10.1093/treephys/tpaa064.
Verhertbruggen Y, Walker JL, Guillon F, Scheller HV. 2017. A comparative study of sample preparation for staining and immunodetection of plant cell walls by light microscopy. *Front. Plant Sci.* 8: 1505. DOI: 10.3389/fpls.2017.01505.
Wear DN, Greis JG. 2012. The southern forest futures project: summary report. Gen. Tech. Rep. SRS-GTR-168. USDA-Forest Service, Southern Research Station, Asheville, NC. DOI: 10.2737/srs-gtr-168.
Wiedenhoeft AC, Miller RB. 2002. Brief comments on the nomenclature of softwood axial resin canals and their associated cells. *IAWA J.* 23: 299–303. DOI: 10.1163/22941932-90000305.
Wimmer R, Grabner M. 1997. Effects of climate on vertical resin duct density and radial growth of Norway spruce [*Picea abies* (L.) Karst.]. *Trees* 11: 271–276. DOI: 10.1007/PL00009673.
Wimmer R, Grabner M, Strumia G, Sheppard PR. 1999. Significance of vertical resin ducts in the tree rings of spruce. In: R Wimmer, Vetter RE (eds.), *Tree-ring analysis: biological, methodological and environmental aspects*: 107–118. CABI Publishing, Wallingford.
Wu H, Hu ZH. 1997. Comparative anatomy of resin ducts of the Pinaceae. *Trees* 11: 135–143. DOI: 10.1007/s004680050069.
Yan F, Zhang H, Kube CR. 2005. A multistage adaptive thresholding method. *Pattern Recognit. Lett.* 26: 1183–1191. DOI: 10.1016/j.patrec.2004.11.003.
Yang JL, Downes G, Chen F, Cown D. 2006. Investigation of within-tree and between-site resin canal variation. WQI Report APP-64. WQI, New Zealand.
Yoo JC, Han TH. 2009. Fast normalized cross-correlation. *Circuits Syst. Signal Process.* 28: 819–843. DOI: 10.1007/s00034-009-9130-7.
Zhang C, Fujii T, Abe H, Fujiwara T, Fujita M, Takabe K. 2008. Anatomical features of radial resin canals in *Pinus densiflora*. *IAWA J.* 29: 179–187. DOI: 10.1163/22941932-90000178.
Zhang X. 2022. Two-step non-local means method for image denoising. *Multidimens. Syst. Signal Process.* 33: 341–366. DOI: 10.1007/s11045-021-00802-y.
Zhao S, Erbilgin N. 2019. Larger resin ducts are linked to the survival of lodgepole pine trees during mountain pine beetle outbreak. *Front. Plant Sci.* 10: 471911. DOI: 10.3389/fpls.2019.01459.